

Controlled heterogeneous water distribution and evaporation towards enhanced photothermal water-electricity-hydrogen production

Yi Zhou^{a,b,1}, Tianpeng Ding^{a,1}, Minmin Gao^a, Kwok Hoe Chan^a, Yin Cheng^a, Jiaqing He^b, Ghim Wei Ho^{a,c,*}

^a Department of Electrical and Computer Engineering, National University of Singapore, 4 Engineering Drive 3, 117583, Singapore

^b Department of Physics, Southern University of Science and Technology, Shenzhen, 518055, China

^c Institute of Materials Research and Engineering, A*STAR (Agency for Science, Technology and Research), 3 Research Link, 117602, Singapore

ARTICLE INFO

Keywords:

Photothermal interfacial water evaporation
Multiscale structure manipulation
Thermoelectric energy harvesting
Water-electricity-hydrogen production

ABSTRACT

The ability to control heterogeneous water distribution and evaporation could address low vapor generation issues which has great implications for distillation and energy systems efficiency. Herein, we devise an efficient solar-driven water-electricity-hydrogen generation system by spatially controlling water diffusion and evaporation of 3D hydrogel evaporators. Specifically, through template-assisted regulation of the interfacial structures of the hydrogel evaporator, the relationship between the macroscale liquid-vapor area and the water pumping pathway was studied. The hybrid wettability and distinct water distribution strategy achieved via selective hydrophobic-hydrophilic modification enhance the photothermal efficiency by 207% compared with the flat hydrophilic evaporator. Finally, the tailored hydrogels for contrasting evaporative cooling and solar absorption heating are integrated with Bi₂Te₃-based thermoelectric generator (TEG) to efficiently convert waste heat into electricity and drive electrochemical water splitting under outdoor sunny/cloudy conditions. The prototype demonstrates evaporation of 1.42 kg m⁻² h⁻¹, power output of 4.8 W/m², and hydrogen evolution of 0.3 mmol/h. This work could pave the development of highly integrated hybrid systems to deliver three crucial water, energy and fuel commodities for global sustainability.

1. Introduction

Water, energy, and fuels are three essential elements pertaining to sustainability, economic growth, and societal development. Solar-driven water evaporation, which utilizes renewable sunlight as a promising approach to tackle the scarcity of clean water [1–7], has also been used to drive other processes, such as solar desalination [8–10], water harvesting and purification [11–13], power generation [14–16], salt harvesting/rejection [17,18] and photothermal catalysis [19,20]. To date, the photothermal water evaporation system focuses mainly on interfacial steam generation where the heat is localized at the water/air interface for vapor generation without large heat losses, making it an efficient approach compared to traditional bottom-up and volumetric heating [21–23]. Nevertheless, it is difficult to strike a delicate balance between the amount of water on the evaporator surface that is pumped from the bulk water and the interfacial heating of the evaporator. Explicitly, at constant solar intensity, a thick water layer from fast water

pumping rate adversely decreases the evaporation temperature, whereas slow water diffusion results in undesired dehydration of solar evaporator and heat penetration into bulk water. Accordingly, optimal water pumping rate to maximize interfacial heating is critical for highly efficient solar vaporization and energy utilization.

Aside from the solar-driven steam generation, integrated water desalination and waste energy harvesting have also attracted tremendous attention as it represents an eco-friendly approach to solve the inextricably interdependent water and energy shortage simultaneously, as opposed to conventional segregated water heating and energy harvesting solutions [24–26]. Increasingly more works are reported on energy generation coupled to the water evaporation process in recent years, which is primarily driven by the energy flow across the evaporation system and waste energy harvesting. For instance, ionvoltaic cells convert the water evaporation-induced ion concentration gradient, between the seawater and evaporation surface, into electricity using selective membranes and electrodes [27,28]. Besides that, the random

* Corresponding author. Department of Electrical and Computer Engineering, National University of Singapore, 4 Engineering Drive 3, 117583, Singapore.
E-mail address: elehw@nus.edu.sg (G.W. Ho).

¹ These authors contributed equally: Y. Zhou and T. Ding.

<https://doi.org/10.1016/j.nanoen.2020.105102>

Received 17 April 2020; Received in revised form 3 June 2020; Accepted 17 June 2020

Available online 15 July 2020

2211-2855/© 2020 Elsevier Ltd. All rights reserved.

kinematics of vapors and condensed droplets resulting from the respective water evaporation and condensation are scavenged by piezoelectric/triboelectric generators [29,30]. Also, thermoelectric, pyroelectric, and thermogalvanic generators are coordinated with solar absorber to harvest waste heat and augment the photothermal efficiency [31–34]. Moreover, photovoltaic (PV) cells are integrated with the water evaporation system for sunlight energy conversion and thermal management [35–37]. Needless to say, the future needs for uncompromised solar-driven clean water and energy integrated solutions with high energy utilization under all-weather conditions are of paramount importance yet rarely reported. Consequently, it is necessary to develop new approaches that not only enhance the photothermal utilization for clean water supply but also facilitate the diversification of energy production i.e. electricity and green fuel.

Herein, we devise a spatially confined inhomogeneous water diffusion and interfacial heating of 3D pillar evaporators to demonstrate solar water-electricity-hydrogen production prototype for the synergistic generation of clean water and energy. Taking the approach of materials engineering, the polyacrylamide (PAM)/carbon nanotube (CNT) hydrogel-based solar absorbers are investigated from the projection ratio (the cross-sectional water pathway area relative to the total evaporating surface area), water spreading, to hydrophilic/hydrophobic wettability for enhanced solar vaporization. Apart from solar-driven water evaporation, evaporative cooling of the tailored hydrogel and waste solar-thermal energy are directly harvested by Bi_2Te_3 -based TEG to produce electricity and achieve self-powered hydrogen production. This study offers a feasible solution to convert distributed ambient energy concurrently into clean water and energy under multi-situation conditions with minimum environmental impact.

2. Results and discussions

The design concept of multiscale structure manipulation for solar-driven water-electricity-hydrogen production is schematically depicted in Fig. 1. This system consists of a hydrogel-based solar absorber/evaporator, a thermoelectric energy harvester, and a water splitting device. From a macroscale view, the bi-functional hydrogel prepared with polyacrylamide (PAM) and carbon nanotube (CNT) serves both as a solar absorber and a water evaporator. Besides, thermoelectric energy harvesters are integrated with the hydrogel-based water evaporator and solar absorber to scavenge waste heat to electricity and power electrolysis of water. As illustrated in Fig. 1, for solar vaporization, the hydrophilic hydrogel absorber/evaporator is systematically optimized from macro/microscale to molecular network. Specifically, 3D pillar

structures are introduced to modulate the projection ratio and liquid-vapor interfacial area, efficiently regulating the water and heat distributions and enhancing the interfacial water evaporation rate. On the other hand, hybrid wettability from the hydrophilic water pathway and selective hydrophobic surface modifications of PAM/CNT hydrogels are designed to synergistically promote the water diffusion and evaporation. Ultimately, the delicate structural manipulations lead to a multifunctional hydrogel absorber/evaporator which offers a feasible route to clean water and clean energy production.

2.1. Macro/microscale structure manipulations

Carbon nanotubes and polyacrylamide are composited and utilized for mold-assisted pillar fabrication of an array of 3D solar absorber/evaporator that is of high flexibility, lightweight and anti-oil fouling (Fig. 2a–c). The hydrophilic molecular chains and porous skeleton of PAM hydrogel ensure effective water pumping and storage for evaporation [38]. The preparation procedure of hydrogel-based evaporator/absorber using various template geometries is presented (Experimental Section, Supplementary Information, Figs. S1 and S2). The optical absorption for solar absorbers is characterized in Fig. 2d, where the evaporator prepared with hydrophilic PAM/CNT and hydrophobic PAM/CNT/FOTS (modified with 1H,1H,2H,2H-perfluorooctyl trichlorosilane, FOTS) show preferable full-spectrum solar absorption compared to pure PAM.

As mentioned, determining an equilibrium in the water pumping rate and interfacial heating is essential to conceive intense and localized hotspots. Hence, to find the optimal balance between water diffusion and interfacial heating at the liquid/vapor interface, PAM/CNT hydrogel (PCH, the weight ratio of CNT: PAM is 1.5: 100) absorbers/evaporators with various 3D pillar dimensions are designed and fabricated (flat, pillar $d_1 \times h_2$, pillar $d_2 \times h_2$, pillar $d_3 \times h_2$; unit: diameter (mm) \times height (mm), denoted as FPCH, PCH1, PCH2, PCH3), as shown in Fig. 2e and S2. From the perspective of interfacial heating, the projected area (A_1) and total liquid/vapor interfacial area ($A_1 + A_2$) of the device are two critical factors influencing the water evaporation and are mainly dependent on the 3D structures and wettability of the solar absorber, as well as the water surface tension (Supplementary Note S1). A_2 stands for the sidewall of the total pillars and the substrate surface area excluding the projected area. The solar absorber containing pillars with a diameter/height of 2 mm (PCH2) possesses the highest projection ratio ($A_1 / (A_1 + A_2)$) compared to other designs (Fig. 2e, the theoretical calculation is presented in Supplementary Note S1). The evaporation performance of solar evaporators with various pillar dimensions is evaluated under 1-

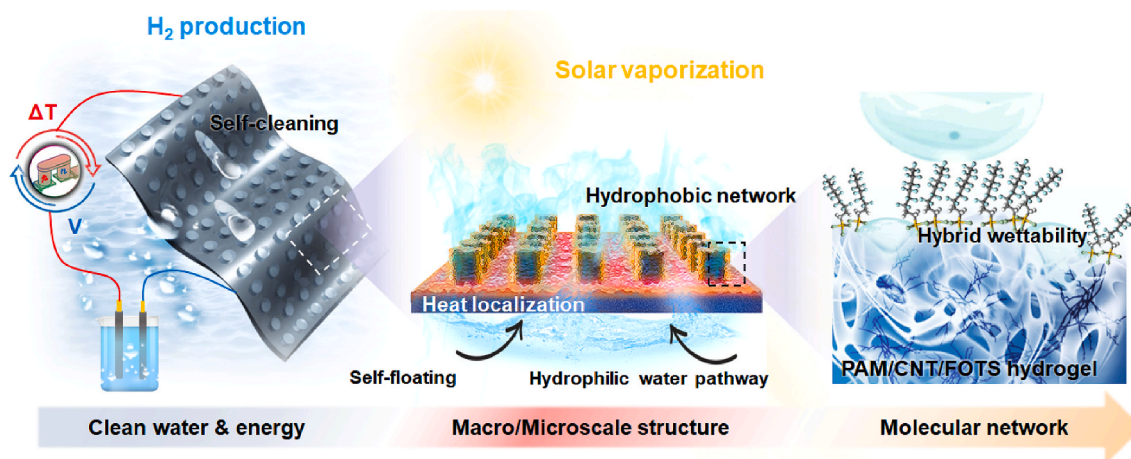


Fig. 1. Schematic of the photothermal water-electricity-hydrogen co-production system and beyond solar-driven interfacial water evaporation. Design concept and multiscale structure manipulation of solar absorber/evaporator for enhanced interfacial evaporation for synergistic solar water, thermoelectricity, and water electrolysis.

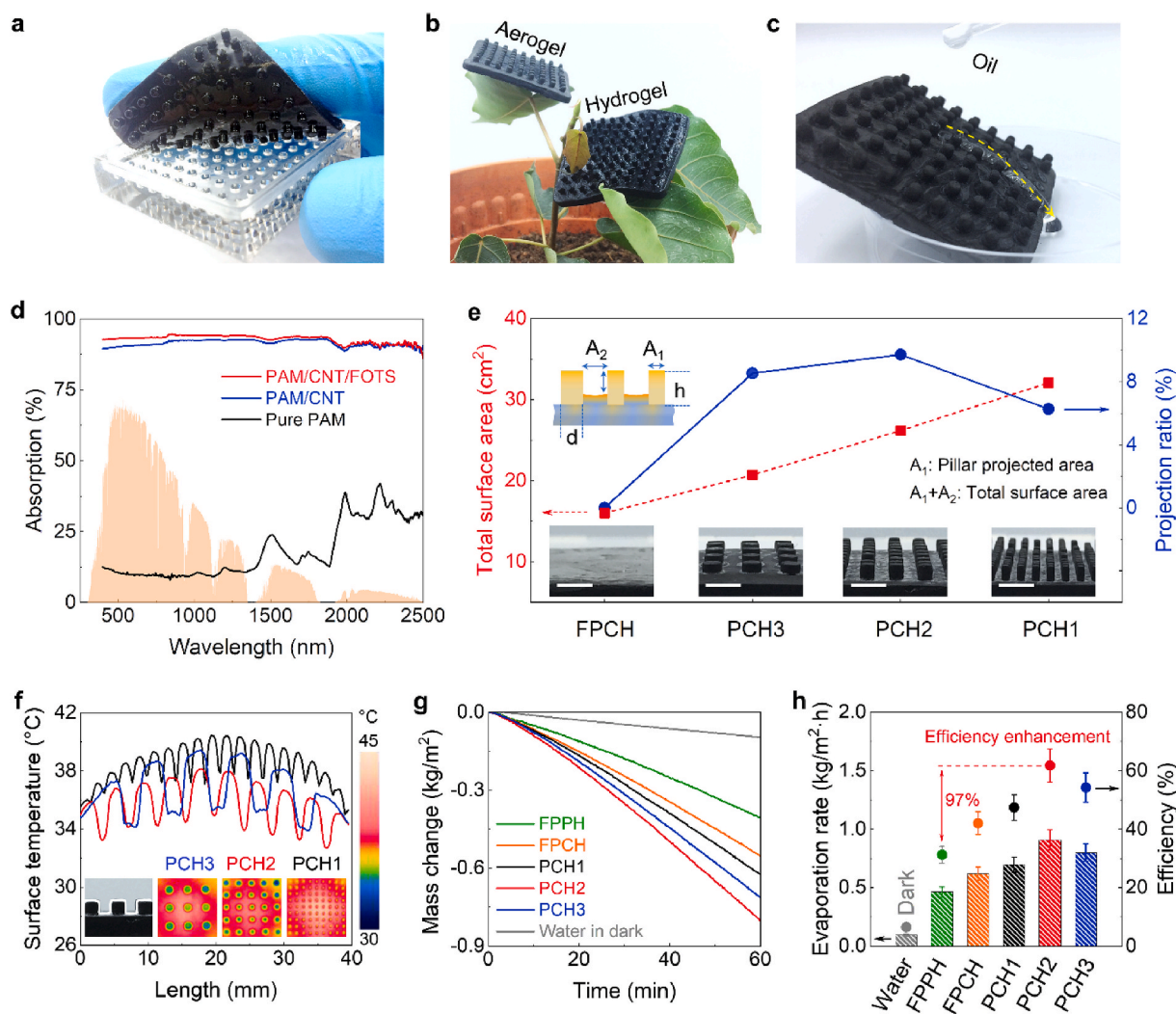


Fig. 2. Characterization of pillar structured hydrogel evaporator. (a) Flexible, (b) lightweight and (c) anti-oil fouling aerogel/hydrogel. (d) Optical light absorption for various water evaporators. (e) Total surface area and projection ratio calculated for above and below liquid/vapor interface with different pillar dimensions. Scale bar: 5 mm. (f) Surface temperature of the solar evaporators with various pillar dimensions. (g) Water mass change and (h) evaporation rate as well as photothermal efficiency evaluation under one sun intensity.

sun (Fig. 2f–h). The disparities of periodical surface temperature fluctuation of the various pillar-based solar absorbers (Fig. 2f) elucidate distinct water-evaporation state at the interface, which results in different mass changes (Fig. 2g) as well as evaporation rates and photothermal efficiencies (Fig. 2h). Also, the temperature of the central area for the solar absorber is slightly higher than that of the marginal area (Fig. 2f), which mainly results from the simulated sunlight intensity distribution of Xe lamp and center-to-edge solar heat convection. Compared with a flat solar absorber substrate, the pillars exhibit lower temperatures. The evaporation of heterogeneously distributed water on the large surface area pillared structures is more vigorous than that of the flat liquid/vapor interface. Besides, due to the temperature difference between the pillar and substrate, the water evaporation from the pillar structure is further facilitated by thermocapillary force or heat-induced Marangoni effect [39]. These results are consistent with the projection ratio in Fig. 2e and verified by various pillar dimensions in Fig. 2f. The measured mass change of PCH2 solar evaporator shows a maximum photothermal efficiency of 61% (Supplementary Note S2), which equates to a 97% increase over conventional flat pure PAM hydrogel (FPPH) solar absorber. Moreover, the evaporation performance of the solar absorbers with different pillar heights with and without 1-sun irradiation (Figs. S3 and S4) are characterized as well,

providing further verification that the pillared 3D-structure manipulation is advantageous for interfacial water evaporation.

Aside from the modulation of water distribution and effective interfacial heating at liquid/vapor interface through macroscale pillar structures, the microscale porous structure comprising pore size and water pathway confinement in hydrogel-based evaporator also affect the interfacial water evaporation. The evaporating performance declines when the height/diameter ratio of the pillars (e.g., PCH1, PCH23, Table S1) gets too large. This mainly results from the dehydration of the hydrogels caused by low water pumping and diffusion in the solar evaporator. Based on the optimum pillar dimension design (i.e. PCH2), the CNT: PAM weight proportion of the solar absorber/evaporator is varied to control the micropore structure and facilitate water pumping. Fig. 3a and b and S5 present the pore size distribution and morphology for porous PAM/CNT hydrogel-based evaporator (PPCH) with CNT: PAM weight ratio of 1.5: 100, 1.5: 50, and 1.5: 25 (denoted as PPCH1 (i.e. PCH2), PPCH2 and PPCH3). The hydrogel with a weight ratio of 1.5: 25 (PPCH3) shows the largest average pore size (10.62 μm), most favorable for water absorption, pumping, and storage (Fig. S6). The corresponding evaporation performance for various weight ratios is shown in Fig. 3c–e. The optimal PPCH3 solar evaporator with a weight ratio of 1.5: 25 presents lower average surface temperature and higher

water mass change, compared with other solar evaporators. Notably, the total photothermal efficiency of the solar evaporator is enhanced by 34.3%, and the peak value achieved is around 82%. Though further reduction of the PAM weight ratio to be lower than 1.5: 25 may lead to a higher water evaporation rate, it compromises mechanical properties. On the basis of the experimental observations, the manipulation of the macro/microscale structure of solar absorber unambiguously offers a possible means to modulate the water diffusion both at the evaporator and at the liquid/vapor interface, to attain a fine balance between the water supply and interfacial vaporization.

2.2. Molecular-network-based hybrid wettability

With respect to solar-driven vaporization, the afore discussed macro/microscale evaporator structural manipulations have successfully achieved high-efficiency energy utilization. Nonetheless, the high-water storage capability and surface tension of the porous hydrophilic evaporator (i.e. PPCH3) leads to an excessive thick water layer residing on the evaporator, which diminishes self-floating capability (Fig. 3d and the inset shows foam is used to float the PPCH3 evaporator). This high surface tension and low water distribution controllability decrease the interfacial heating process and hence results in a low evaporation rate (Fig. 2g, h, 3d, and 3e). The typical approach towards self-floating solar evaporator is to introduce hydrophobic materials into the evaporator design, forming a bilayer structure [40–42]. Unfortunately, the introduction of the hydrophobic layer deprives the water evaporation performance, as the hydrophilic pathway is hindered [25,43], leading to insufficient water pumping.

Thereby, wettability manipulation at liquid/vapor interface for controllable surface tension and water diffusion, as well as enhanced interfacial water evaporation was undertaken. The hydrophilic porous PPCH3 evaporator is tuned hydrophobic through the judicious incorporation of 1H,1H,2H,2H-perfluorooctyl trichlorosilane (FOTS) into the molecular network, as shown in Fig. 4a and S7. The modified regions of hydrophobic PAM/CNT hydrogel (hPCH), to a certain extent, are identified by fluorine mapping mostly at the boundary of the pores (Fig. S7c),

whereas the inner area of micropores remained largely hydrophilic to serve as water pumping pathway (Figs. S7c and S7d). The detailed surface modification process is described in Supplementary Information, and the mechanism for the wettability manipulation is explicated in Fig. 4a [43–45]. Due to molecular deposition and hydrogen bond interaction, the condensation reaction between -Si-O-H and -O-H leads to covalent bond reconstruction, creating the hydrophobic molecule with fluorine chain [46–48]. Moreover, the actualization of selective wettability is mainly attributed to the outmost molecular hydrophobic modification [49], whereas the micropores inside are not effectively modified by FOTS because of the effective barrier formed by the dense outmost network, which can be verified by the hybrid wettability in selected specific regions, as shown in the contact angles (0 and 133°, Fig. 4b) and Supplementary Video S1. As a result, heterogeneous water diffusion and distribution at the interface is realized and the water pumping path from bulk water to liquid/vapor interface is retained. The water spreading on the evaporator/air interface is primarily dependent on the surface tension difference of hydrophilic/hydrophobic porous hydrogel. The thick water layer from the hydrophilic region spreads into the hydrophobic area and forms a water film due to the high surface molecular interaction. The thin water film is ideal for interfacial water evaporation, which can be further promoted by the solute-induced Marangoni effect between hydrophilic/hydrophobic areas [50].

Supplementary data related to this article can be found at <https://doi.org/10.1016/j.nanoen.2020.105102>.

The advantages of hybrid wettability of hydrophilic/hydrophobic hydrogel-based evaporator (hPCH) are experimentally verified (Fig. 4c–e). The solar absorber temperature of the hPCH evaporator is lower than the typical hydrophilic PPCH3 evaporator (Fig. S8), and the heat penetration for hydrophobic evaporator is also suppressed (Fig. S8c). Also, the water mass changes for hydrophobic evaporator (hPCH) is more significant than that of the unprocessed hydrogel (PPCH3) (Fig. 4c and S8a). Furthermore, the hydrogel-based water evaporators with (hPCH) and without hydrophobic (PPCH3) modification are investigated for salt-rejection (Fig. 4c–e and S9). The hPCH evaporator presents higher water mass change, evaporation rate, and

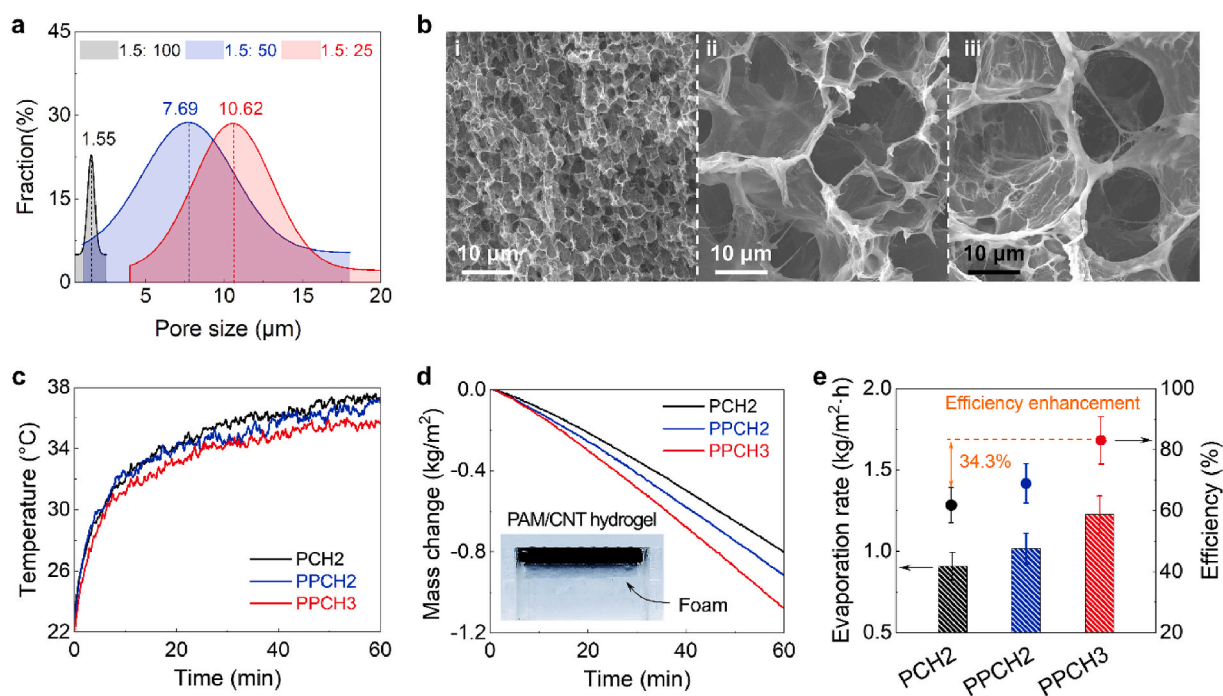


Fig. 3. Microscale porous structure manipulations for enhanced interfacial water evaporation. (a) Pore size distribution and (b) morphology of porous structures with CNT: PAM weight ratio of i) 1.5: 100, ii) 1.5: 50, and iii) 1.5: 25. (c) Temperature increase and (d) water mass change as well as (e) evaporation rate and photothermal efficiency for PAM/CNT-based 3D structured evaporator with $d_2 \times h_2$ pillars under various CNT vs. PAM weight ratios and one sun intensity.

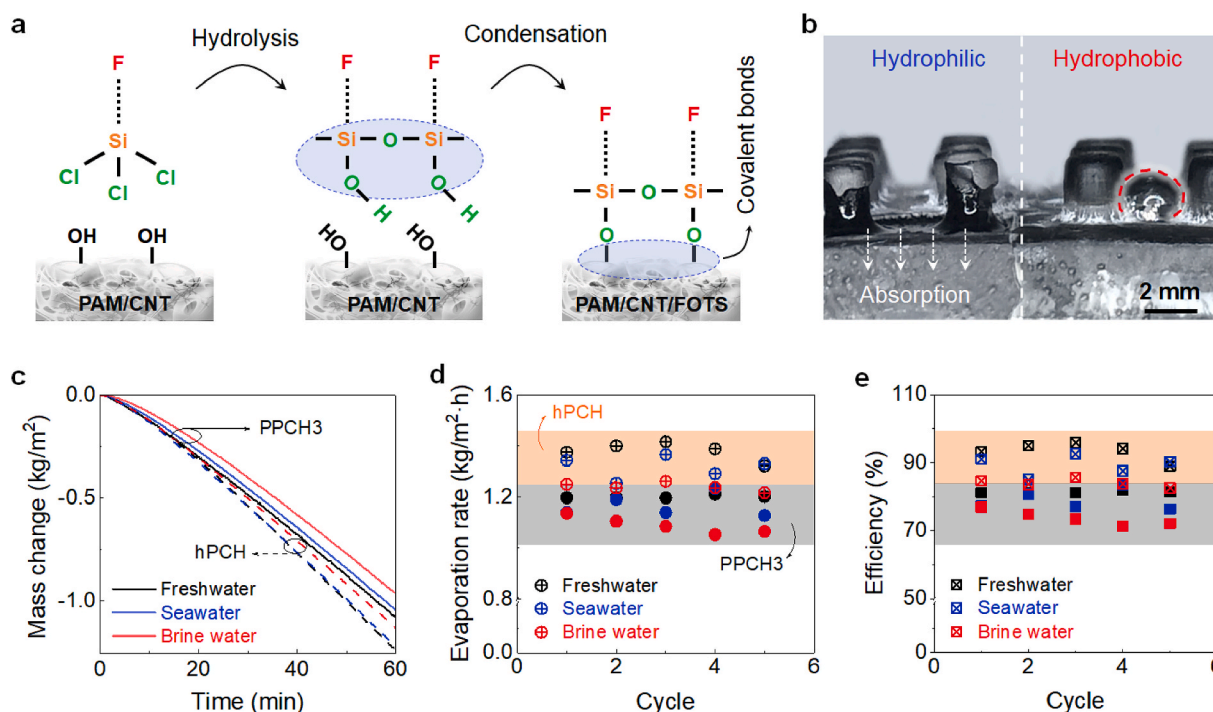


Fig. 4. Mechanism and performance evaluation of selective hydrophilic/hydrophobic wettability evaporators. (a) Schematic illustration of the hydrophobic modification and crosslinking mechanism. (b) Contact angle tests of PAM/CNT-based hydrophilic and PAM/CNT/FOTS-based hydrophobic hydrogels. Performance evaluation of (c) mass change, (d) water evaporation rate and (e) photothermal efficiency with and without hydrophobic modifications using freshwater ($\sim 0\%$), seawater (~ 3.5 wt%) and brine water (~ 20 wt%) at one sunlight intensity.

photothermal efficiency under various salt concentrations ($\sim 0\%$ freshwater, ~ 3.5 wt% seawater, ~ 20 wt% brine water), compared with PAM/CNT-based hydrophilic evaporator at a 1-sun intensity as well as other solar-evaporation systems (Fig. S10). Additionally, both hydrophilic and hydrophobic hydrogel water evaporators exhibited fairly stable evaporation performance (Fig. 4d–e). In particular, the hybrid wettability is operable not only for the photothermal vaporization under various sunlight intensities (Figs. S8a and S11) but also in dark (Fig. S12). Ultimately, multiscale engineering of the hydrogel-based solar evaporator shows a photothermal efficiency of 96% with an enhancement of 207% compared with the usual flat pure PAM-based solar evaporator (Fig. S13). Moreover, the introduction of hydrophobic monomers into the hydrogel evaporator enhances its mechanical strength (Fig. S14) [38]. This overcomes the prevalent low mechanical strength and brittleness of the conventional hydrogels for practical applications.

2.3. Solar water-electricity-hydrogen production

To improve the solar energy utilization, waste heat from the evaporation device is harvested by commercial bismuth telluride thermoelectric materials, and the as-generated electricity is further used to power water electrolysis to produce hydrogen (Fig. 5a and b). Fig. 5b demonstrates a solar water-electricity-hydrogen prototype, where pillared ($d_2 \times h_2$) pure PAM hydrogels with low weight ratio (1.5: 25) and hydrophobic modification (hPPH, Fig. 5b(i)) are utilized as the solar evaporator to evaporatively cool the thermoelectric generator (TEG, Fig. 5b(ii)). Meanwhile, flat PAM/CNT hydrophilic hydrogels with high-efficient heat absorption serve as the solar absorber/evaporator (Fig. 5b (iii)) to heat the other side of the TEG array. The home-made TEG fabrication process is illustrated in Fig. S15 [51,52]. The water mass change of 14.2 g is obtained under 3-h fluctuating solar irradiation (Fig. 5c). The TEG array generates 2.8 V under 55 °C temperature difference (Figs. 5d), and 4.8 W/m² maximum power density under a matched load resistor (32 Ω) (Supplementary Note S3). An energy

harvesting (EH) circuit consisting of a diode (0.5 V consumption) and a supercapacitor (5.3 V, 1.0 F) is directly connected with the TEG array to stabilize the voltage output (Fig. 5d and S16), with the water splitting setup serially connected for continuous hydrogen production (Fig. 5b (iv) and (v)). The measured gas shows a hydrogen production rate of 0.3 mmol/h (Fig. 5e), and continuous bubbling is observed for the entire test duration (Supplementary Video S2). A comparison of the photothermal water evaporation and thermoelectric energy harvesting of integrated solar water-electricity generators to the other reported designs is presented in Fig. S17.

Supplementary data related to this article can be found at <https://doi.org/10.1016/j.nanoen.2020.105102>.

3. Conclusion

In summary, we have devised a hydrogel-based solar-driven water-electricity-hydrogen co-production system for enhanced photothermal energy utilization by systematically controlling heterogeneous water distribution and evaporation. The 3D pillared PAM/CNT hydrogel with selected hydrophobic modification balanced the water pumping ability and evaporating rate, and facilitated the heat localization effect at the liquid/vapor interface. This leads to enhanced interfacial solar-driven water evaporation of $\sim 96\%$ photothermal efficiency. The integral design of the synergistic generation of clean water and energy under natural conditions was also demonstrated. Thermoelectric generators serve as thermal insulators sandwiched by pure PAM-based evaporators and PAM/CNT-based solar absorbers for cooling and heating respectively. Continuous electrical output of 4.8 W/m² with a power management circuit is delivered to drive water splitting and produce hydrogen of 0.3 mmol/h. This work is of great significance for solar-driven steam generation as well as energy crisis and environmental pollution remediations.

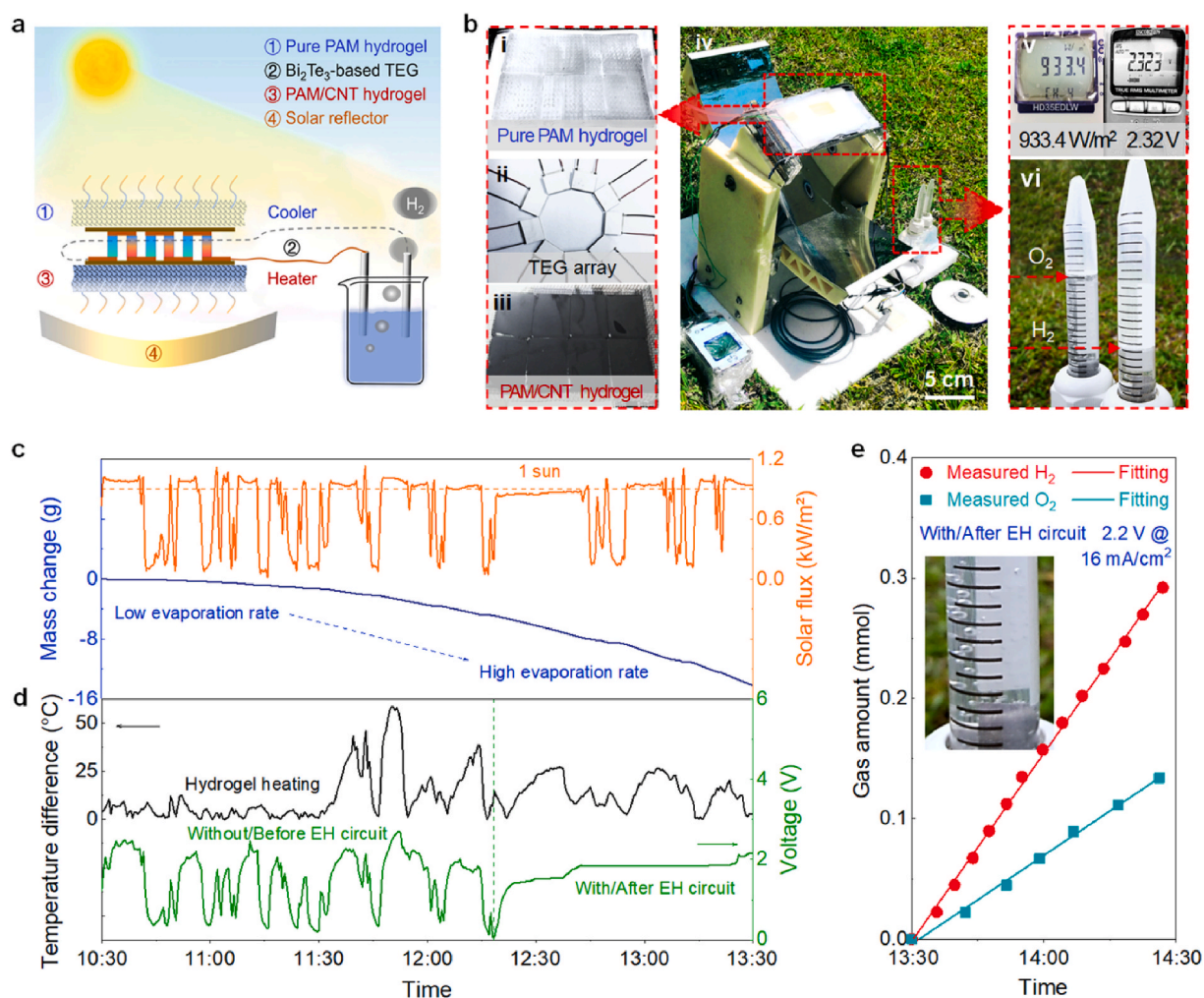


Fig. 5. Outdoor demonstration for solar water-electricity-hydrogen co-production. (a) Schematic diagram and (b) prototype for the synergetic generation of clean water and energy. (c) Water evaporation mass change as a function of solar flux. (d) Temperature difference measured from the hot-side (heated by PAM/CNT hydrogel-based absorber) and cold-side (cooled by pure PAM hydrogel-based evaporator) of TEG array, as well as output voltage. The energy harvesting (EH) circuit is integrated with TEG array to stabilize the electricity output and drive water electrolysis. (e) The plot of hydrogen and oxygen evolution. The inset shows generated hydrogen bubbles.

Declaration of competing interest

The authors declare that they have no known competing financial interests or personal relationships that could have appeared to influence the work reported in this paper.

CRediT authorship contribution statement

Yi Zhou: Conceptualization, Methodology, Software, Formal analysis, Writing - original draft. **Tianpeng Ding:** Conceptualization, Methodology, Formal analysis, Visualization, Writing - original draft. **Minmin Gao:** Visualization, Investigation. **Kwok Hoe Chan:** Resources, Investigation. **Yin Cheng:** Resources, Investigation. **Jiaqing He:** Supervision. **Ghim Wei Ho:** Formal analysis, Writing - review & editing, Supervision.

Acknowledgments

This work was supported by the Ministry of Education (MOE) under Grant Nos. R-263-000-D18-112 and R-263-000-C85-112.

Appendix A. Supplementary data

Supplementary data to this article can be found online at <https://doi.org/10.1016/j.nanoen.2020.105102>.

References

- [1] I.E. Agency, Global Energy & CO₂ Status Report 2018, OECD/IEA, 2019.
- [2] I.E. Agency, Market Report Series: Energy Efficiency 2018, OECD/IEA, 2018.
- [3] Q. Schiermeier, J. Tollefson, T. Scully, A. Witzke, O. Morton, *Nature* 454 (2008) 816–823.
- [4] Y. Pang, J. Zhang, R. Ma, Z. Qu, E. Lee, T. Luo, *ACS Energy Lett.* 5 (2020) 437–456.
- [5] C. Chen, Y. Kuang, L. Hu, *Joule* 3 (2019) 683–718.
- [6] Y. Tu, R. Wang, Y. Zhang, J. Wang, *Joule* 2 (2018) 1452–1475.
- [7] Z. Xu, L. Zhang, L. Zhao, B. Li, B. Bhatia, C. Wang, K.L. Wilke, Y. Song, O. Labban, J.H. Lienhard, R.Z. Wang, E. Wang, *Energy Environ. Sci.* 13 (2020) 830–839.
- [8] S. He, C. Chen, Y. Kuang, R. Mi, Y. Liu, Y. Pei, W. Kong, W. Gan, H. Xie, E. Hitz, C. Jia, X. Chen, A. Gong, J. Liao, J. Li, Z.J. Ren, B. Yang, S. Das, L. Hu, *Energy Environ. Sci.* 12 (2019) 1558–1567.
- [9] Y. Kuang, C. Chen, S. He, E.M. Hitz, Y. Wang, W. Gan, R. Mi, L. Hu, *Adv. Mater.* 31 (2019) 1900498.
- [10] C. Li, D. Jiang, B. Huo, M. Ding, C. Huang, D. Jia, H. Li, C.Y. Liu, J. Liu, *Nano Energy* 60 (2019) 841–849.
- [11] Y. Guo, H. Lu, F. Zhao, X. Zhou, W. Shi, G. Yu, *Adv. Mater.* 32 (2020) 1907061.
- [12] X. Zhou, F. Zhao, Y. Guo, B. Rosenberger, G. Yu, *Sci. Adv.* 5 (2019), eaaw5484.
- [13] F. Zhao, X. Zhou, Y. Liu, Y. Shi, Y. Dai, G. Yu, *Adv. Mater.* 31 (2019) 1806446.
- [14] J. Li, K. Liu, T. Ding, P. Yang, J. Duan, J. Zhou, *Nano Energy* 58 (2019) 797–802.

- [15] G. Xue, Y. Xu, T. Ding, J. Li, J. Yin, W. Fei, Y. Cao, J. Yu, L. Yuan, L. Gong, J. Chen, S. Deng, J. Zhou, W. Guo, *Nat. Nanotechnol.* 12 (2017) 317–321.
- [16] T. Ding, K. Liu, J. Li, P. Yang, Q. Chen, G. Xue, J. Zhou, *Chin. Sci. Bull.* 63 (2018) 2846–2852.
- [17] Y. Xia, Q. Hou, H. Jubaer, Y. Li, Y. Kang, S. Yuan, H. Liu, M.W. Woo, L. Zhang, L. Gao, H. Wang, X. Zhang, *Energy Environ. Sci.* 12 (2019) 1840–1847.
- [18] G. Ni, S.H. Zandavi, S.M. Javid, S.V. Boriskina, T.A. Cooper, G. Chen, *Energy Environ. Sci.* 11 (2018) 1510–1519.
- [19] L. Zhu, M. Gao, C.K.N. Peh, G.W. Ho, *Mater. Horiz.* 5 (2018) 323–343.
- [20] M. Gao, C.K. Peh, L. Zhu, G. Yilmaz, G.W. Ho, *Adv. Energ. Mater.* 10 (2020) 2000925.
- [21] Z. Wang, Y. Liu, P. Tao, Q. Shen, N. Yi, F. Zhang, Q. Liu, C. Song, D. Zhang, W. Shang, T. Deng, *Small* 10 (2014) 3234–3239.
- [22] H. Ghasemi, G. Ni, A.M. Marconnet, J. Loomis, S. Yerci, N. Miljkovic, G. Chen, *Nat. Commun.* 5 (2014) 4449.
- [23] G. Ni, G. Li, Svetlana V. Boriskina, H. Li, W. Yang, T. Zhang, G. Chen, *Nat. Energy* 1 (2016) 16126.
- [24] M. Gao, L. Zhu, C.K. Peh, G.W. Ho, *Energy Environ. Sci.* 12 (2019) 841–864.
- [25] P. Tao, G. Ni, C. Song, W. Shang, J. Wu, J. Zhu, G. Chen, T. Deng, *Nat. Energy* 3 (2018) 1031–1041.
- [26] L. Zhu, M. Gao, C.K.N. Peh, G.W. Ho, *Nano Energy* 57 (2019) 507–518.
- [27] P. Yang, K. Liu, Q. Chen, J. Li, J. Duan, G. Xue, Z. Xu, W. Xie, J. Zhou, *Energy Environ. Sci.* 10 (2017) 1923–1927.
- [28] B. Hou, D. Kong, J. Qian, Y. Yu, Z. Cui, X. Liu, J. Wang, T. Mei, J. Li, X. Wang, *Carbon* 140 (2018) 488–493.
- [29] L. Zhu, M. Gao, C.K.N. Peh, X. Wang, G.W. Ho, *Adv. Energ. Mater.* 8 (2018) 1702149.
- [30] M. Gao, C.K. Peh, H.T. Phan, L. Zhu, G.W. Ho, *Adv. Energ. Mater.* 8 (2018) 1800711.
- [31] L. Zhu, T. Ding, M. Gao, C.K.N. Peh, G.W. Ho, *Adv. Energ. Mater.* 9 (2019) 1900250.
- [32] X. Li, X. Min, J. Li, N. Xu, P. Zhu, B. Zhu, S. Zhu, J. Zhu, *Joule* 2 (2018) 2477–2484.
- [33] T. Ding, L. Zhu, X.-Q. Wang, K.H. Chan, X. Lu, Y. Cheng, G.W. Ho, *Adv. Energ. Mater.* 8 (2018) 1802397.
- [34] J. Duan, G. Feng, B. Yu, J. Li, M. Chen, P. Yang, J. Feng, K. Liu, J. Zhou, *Nat. Commun.* 9 (2018) 5146.
- [35] W. Wang, Y. Shi, C. Zhang, S. Hong, L. Shi, J. Chang, R. Li, Y. Jin, C. Ong, S. Zhuo, P. Wang, *Nat. Commun.* 10 (2019) 3012.
- [36] N. Xu, P. Zhu, Y. Sheng, L. Zhou, X. Li, H. Tan, S. Zhu, *J. Zhu, Joule* 4 (2020) 347–358.
- [37] R. Li, Y. Shi, M. Wu, S. Hong, P. Wang, *Nat. Sustain.* (2020), <https://doi.org/10.1038/s41893-020-0535-4>.
- [38] J. Chen, Y. Ao, T. Lin, X. Yang, J. Peng, W. Huang, J. Li, M. Zhai, *Polymer* 87 (2016) 73–80.
- [39] L. Wu, Z. Dong, Z. Cai, T. Ganapathy, N.X. Fang, C. Li, C. Yu, Y. Zhang, Y. Song, *Nat. Commun.* 11 (2020) 521.
- [40] L. Zhang, B. Tang, J. Wu, R. Li, P. Wang, *Adv. Mater.* 27 (2015) 4889–4894.
- [41] Y. Li, H. Chen, S. Xiao, M.A. Alibakhshi, C.W. Lo, M.C. Lu, C. Duan, *ACS Nano* 13 (2019) 3363–3372.
- [42] Y. Liu, J. Chen, D. Guo, M. Cao, L. Jiang, *ACS Appl. Mater. Interfaces* 7 (2015) 13645–13652.
- [43] Y. Guo, X. Zhao, F. Zhao, Z. Jiao, X. Zhou, G. Yu, *Energy Environ. Sci.* 13 (2020) 2087–2095.
- [44] Y. Li, L. Li, J. Sun, *Angew. Chem. Int. Ed.* 49 (2010) 6129–6133.
- [45] B. Bhushan, D. Hansford, K.K. Lee, *J. Vac. Sci. Technol. A* 24 (2006) 1197–1202.
- [46] L. Treccani, T. Yvonne Klein, F. Meder, K. Pardun, K. Rezwan, *Acta Biomater.* 9 (2013) 7115–7150.
- [47] A. Matin, U. Baig, M.A. Gondal, *Process Saf. Environ. Protect.* 134 (2020) 226–238.
- [48] N.R. Glass, R. Tjeung, P. Chan, L.Y. Yeo, J.R. Friend, *Biomicrofluidics* 5 (2011) 36501–365017.
- [49] Y. Li, C.-Y. Xu, P. Hu, L. Zhen, *ACS Nano* 7 (2013) 7795–7804.
- [50] S. Kim, J. Kim, H.-Y. Kim, *J. Fluid Mech.* 872 (2019) 100–114.
- [51] Y. Zhou, Z. Guo, J. He, *Appl. Phys. Lett.* 116 (2020), 043904.
- [52] Y. Zhou, S. Zhang, X. Xu, W. Liu, S. Zhang, G. Li, J. He, *Nano Energy* 69 (2020) 104397.